Available online at www.sciencedirect.com
SCIENCE DIRECT®
Journal of Structural Biology 147 (2004) 91–101
Journal of Structural Biology
www.elsevier.com/locate/yjsbi

An improved strategy for automated electron microscopic tomography

Qingxiong S. Zheng,[a] Michael B. Braunfeld,[a] John W. Sedat,[b] and David A. Agard[a,b,*]

[a] The Howard Hughes Medical Institute, University of California, San Francisco, CA 94143-2240, USA
[b] The W.M. Keck Advanced Microscopy Laboratory, Department of Biochemistry and Biophysics, University of California, San Francisco, CA 94143-2240, USA

Received 7 November 2003, and in revised form 10 February 2004
Available online 9 April 2004

Abstract

A prediction-based scheme is proposed and implemented for automated electron microscopic tomography. By assuming that the sample follows a simple geometric rotation and that the optical system can be characterized in terms of an offset between the optical and mechanical axes, it is found that the image movement in the x, y, and z directions due to stage tilt can be dynamically predicted with desired accuracy (15 nm in x–y position and 100 nm in focus). Thus, the microscope optical system (beam/image shift and focus) can be automatically adjusted to compensate for the predicted image movement prior to taking the projected image at each tilt angle. As a consequence, it is not necessary to either record additional images for tracking and focusing during the course of data collections or to spend valuable setup time in a lengthy pre-calibration of stage motions. Furthermore, this scheme is also found to tolerate a significant degree of non-eucentricity and to be quite robust in the collection of regular and cryo low-dose images on thin or thick samples even at magnifications greater than 62 000× and angular step as large as 10°. For interested users the software can be freely downloaded for non-profit use at http://www.msg.ucsf.edu/tomography.

Keywords: Tomography; Automated data collection; Transmission electron microscopy; Cryo microscopy

1. Introduction

Electron microscopic tomography (EMT) is ideally suited to the examination of complex three-dimensional biological structures that fall within the very wide gap between atomic structures defined by X-ray crystallography and the more global patterns of organization that can be observed by light microscopy. Because of its versatility, considerable effort has been devoted to the development of EMT in order to facilitate its use by non-experts within the cell biology community. The idea of EMT is straightforward; specimens are tilted over a large angular range (ideally, between ±70°) and imaged at each tilt angle. Three-dimensional (3D) reconstructions are then performed from those projected images. However, a major practical difficulty is the mechanical imperfection of the available goniometer tilt stages and the inability to precisely set the eucentric height of the sample. As a result, specimens can experience significant shifts in the x, y, and z directions during the course of data acquisition. Even with very large CCD imagers, at high magnification (⩾50 000×), the x and y translations can be large enough to shift the specimen out of the field view. Simultaneously, the resulting z shift leads to severe focus changes, making it difficult to generate an accurate 3D reconstruction. Prior to automated EMT, users were required to manually recenter the specimen and readjust focus. Not only was this manual operation inefficient, but it also resulted in a significant increase in electron dose. For some time, automated EMT (Dierksen et al., 1992; Downing et al., 1992; Koster et al., 1992) has endeavored to solve these problems. The central idea is to accurately determine the x, y, and z shifts that result from stage tilting and to then automatically compensate for the x, y shifts using microscope beam and image shift coils and z (focus) shifts by altering the objective lens current.

* Corresponding author. Fax: 1-415-476-1902.
E-mail address: agard@msg.ucsf.edu (D.A. Agard).

1047-8477/$ - see front matter © 2004 Elsevier Inc. All rights reserved.
doi:10.1016/j.jsb.2004.02.005

Although EMT was recognized as a powerful 3D imaging tool in 1968 (DeRosier and Klug, 1968; Hart, 1968), automated systems only became available in the early 1990s, benefiting from the advent of the computer-controlled transmission electron microscopes and scientific grade slow scan CCD cameras (Dierksen et al., 1992, 1993; Koster et al., 1992, 1993). Those early systems sought to automate the tilting, translation, focusing, and image acquisition steps. During the data collection, images taken before and after each tilt were cross-correlated to measure the specimen translation in the x–y plane. The amount of translation was then compensated by adjusting the image and beam shift coils. To attain accuracy better than 1%, the shift correction procedure was typically repeated. Similarly, focus could be measured at each tilt angle using the beam tilt method (Koster et al., 1992) and then reset to the desired value by adjusting the objective lens current. This correction procedure could also be repeated to gain higher accuracy. Through such an automation procedure, a dose savings of as much as 100-fold was achieved. Automation also resulted in a significant time saving (Braunfeld et al., 1994; Koster et al., 1992). However, the extra dose required to monitor the shift and focus changes can amount to 11% of the total dose (Koster et al., 1997).

Given the growing interest in cryo EMT (Baumeister, 2002; Braunfeld et al., 1994; Rath et al., 1997; Steven and Aebi, 2003), minimizing the extra dose involved in auto tracking and focusing procedures becomes critical. So far, two approaches have been proposed to alleviate this. The earlier solution achieved this goal by distributing the ancillary exposures required for the purpose of recentering and refocusing to areas outside the area containing the object to be reconstructed (Dierksen et al., 1992; Grimm et al., 1997; Rath et al., 1997). More recently, Ziese et al. (2002) suggested the possibility of pre-calibrating the image movement in the xy plane (image shifts) and the z direction (focus change) prior to data collection. Those calibration curves would then be employed during data collection to determine the specimen movement that will be compensated. They showed 5-fold speed improvement in data collection compared to the previous EMT approach. A variation of this approach has been adopted by FEI for their commercial tomography software. A fundamental challenge of this approach is the variability in setting the sample eucentricity and potential variability in the pre-calibration curves. Since these procedures begin at one end of the tilt range, errors become irrecoverable as the sample moves rapidly outside of the trackable area.

Ziese et al. (2002) also mentioned that it might be possible to model and thus to predict the overall image movements after a few measurements of image shift and defocus change. Encouraged by this, we have developed an improved strategy that fulfills the need for image tracking and focusing without additional images. The method, based upon the dynamic prediction of image movement in the spatial domain using previously acquired tomographic images is both fast and very robust. By starting at zero tilt, it is possible to simultaneously model and compensate for errors in sample geometry. Only three extra images need to be acquired at low magnification to eliminate stage backlash and center the object prior to data collection as well as to relocate the image for tilting in the opposite direction. There is no need to record any other image for tracking or focusing throughout data collection. Clearly, this is a better scenario in terms of minimizing beam exposure and is thus quite suitable for cryo-tomography. Compared to the approaches proposed so far, this method exempts users from defining tracking and focusing areas (Rath et al., 1997) or extensive pre-calibration of stage movements (Ziese et al., 2002) and thus results in enhanced productivity and simplicity. With our implementation of this prediction-based scheme, we are able to routinely collect cryo low-dose tomographic data sets of thin and thick samples on both our FEI 200 kV T20 microscope equipped with a Gatan cryo-stage, and our FEI G2 Polara 300 kV F30 Helium transmission electron microscope equipped with an energy filter.

2. Geometric model and movement prediction

2.1. Geometric model

It is presumed that the specimen tilt can be modeled as the rotation of a rigid body around a single tilt axis (Ziese et al., 2002). A sketch of this model is given in Fig. 1, where t stands for the tilt axis and n denotes the direction normal to the tilt axis. The sample point P is the characteristic point at which the optical axis and the specimen intersect. At zero degrees tilt, the location of P is represented by (n_0, z_0), where n_0 is the offset between the tilt axis and the optical axis, and z_0, known as non-eucentricity, represents the distance between the sample point and the tilt axis in z direction. In some cases, the tilt axis can be approximated as being parallel to the y-axis of the CCD image (Ziese et al., 2002). This assumption, however, does not hold on our FEI G2 Helium Polara electron microscope that is equipped with an energy filter. We have observed as much as 26° of angular difference between those two axes depending on magnification. Therefore, this approximation is dropped in the following derivation. (x, y) is used to represent the coordinates in the CCD plane. θ is the angle between the y-axis and the tilt axis.

Assume that a specimen starts to tilt at $\alpha = 0°$, where α is the stage tilt angle, the translation of the specimen at any tilt angle relative to the starting angle can be written in the n–z plane as follows:

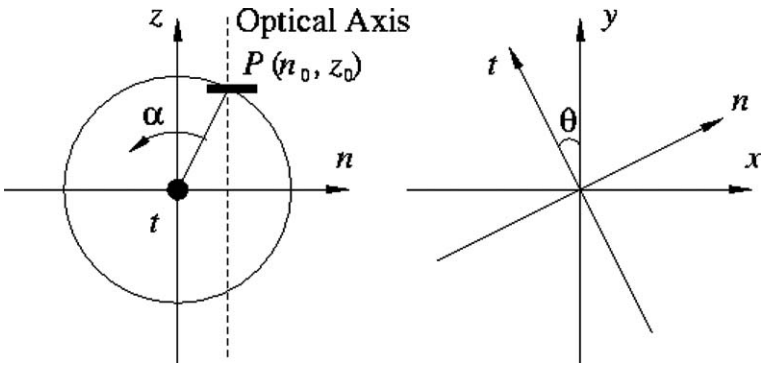

Fig. 1. Geometric model of specimen rotation around tilt axis.

$$\Delta n = n_0 * \cos\alpha + z_0 * \sin\alpha - n_0, \quad (1)$$

$$\Delta z = z_0 * \cos\alpha - n_0 * \sin\alpha - z_0. \quad (2)$$

Since the image movement is measured in the CCD plane, i.e., the x–y plane, the x, y coordinates as functions of tilt angle can be derived by projecting Δn onto x and y axes, separately. This yields Eqs. (3) and (4):

$$\Delta x = n_0 * \cos\theta * \cos\alpha + z_0 * \cos\theta * \sin\alpha - n_0 * \cos\theta, \quad (3)$$

$$\Delta y = n_0 * \sin\theta * \cos\alpha + z_0 * \sin\theta * \sin\alpha - n_0 * \sin\theta. \quad (4)$$

Eqs. (2)–(4), thus fully describe the spatial movement of the sample provided that the unknown geometric parameters (θ, n_0, z_0) can be determined by some means or other. Given this assumption, the sample displacement can thus be predicted instead of being measured for each tilt angle. We can adjust accordingly the optical system to compensate the x, y, and z translations prior to taking a tilt image at each angular step. Because of the explicit dependency on the geometric parameters in the prediction, the values for θ and n_0 need to be determined before data collection, whereas z_0 can be predicted and refined dynamically during data collection.

2.2. Pre-calibration of θ

Using gold beads as alignment fiducial markers, it is possible to very accurately align tilted images (Lawrence, 1992). Experimental results based upon these alignments suggest that the angle of the tilt axis is quite stable between two consecutive microscope alignments, although its value may alter as a function of magnification. θ is then presumed to be a known constant prior to the data collection and its values are pre-calibrated on a suitable test sample for each magnification to be used in data collection. Since the stage x-axis is also the α-tilt axis of the Tecnai Compustage, θ can readily be determined by shifting a calibration sample along the stage x-axis and calculating the angle of the corresponding displacement vector relative to the CCD y-axis. To determine the vector, a pair of images are taken at original and shifted positions and then correlated each other.

2.3. Pre-calibration of n_0

Since n_0 represents the offset between the optical axis and the tilt axis, it should change only very slowly. The physical orientation and location of the tilt axis is expected to remain fixed unless the goniometer is given a service adjustment. The position of the optical axis should also remain relatively unchanged between two consecutive alignments. It is therefore assumed that n_0 can be pre-calibrated and treated as a known constant to predict image movement during data collection. To determine n_0, focus is measured within a range of α tilt angles using the beam tilt method (Koster et al., 1992). Least squares curve fitting to the measured focus values is then applied based upon Eq. (2). Since the focus change is more sensitive to n_0 at lower tilt angles, which can be readily seen from the differentiation of Eq. (2) (see Eq. (5)), the focus measurement can be performed in a range of small tilt angles to estimate n_0. In our implementation, the variation in focus of a thin test specimen was measured every 2° from 0° to 30°.

$$d(\Delta z)/d\alpha = -z_0 * \sin\alpha - n_0 * \cos\alpha. \quad (5)$$

Since significant misalignment of the optical axis to the tilt axis can necessitate large corrections in both large translation and focus, which in turn can lead to image rotation and magnification changes, Ziese et al. (2002) suggested pre-aligning the optical axis to the tilt axis by invoking an appropriate amount of image shift. This capability is provided as an option in our software.

2.4. Dynamic determination of z_0

z_0 denotes the z offset between the object and the tilt axis and can be minimized by setting the eucentric height. Procedures have been developed to automatically adjust sample z height until minimum image movement is detected while the goniometer is wobbling

within a specified angular range. Owing to mechanical imperfections in the goniometer, it is very difficult to tune z_0 to zero. As a result, the uncorrected residue of z_0 can still be severe enough to make the object disappear from the field of view at high magnification and lead to a significant focus change. Furthermore, it is observed that z_0 depends not only on the actual sample being used but also varies from point to point within a sample. This can be attributed to many factors including non-uniform thickness and flatness of the specimen. Hence, z_0 has to be determined dynamically during the course of data collections for each selected sampling point. To do so, note that the usage of Eq. (3) is twofold, meaning that it can also be used to solve for z_0 from the right-hand side based upon a set of data points of (α, Δx). Since n_0 and θ have been pre-determined and are assumed to remain valid until the next microscope alignment, z_0 is the only unknown constant at the right-hand side for a specific sample point. Mathematically, one data point of (α, Δx) is sufficient to solve for z_0. In reality, it is better to use least squares fitting from multiple data points in order to minimize the consequences of errors introduced from measuring the x translation. In our implementation the most recent four data points are used for least squares fitting. Eq. (6) is derived from Eq. (3) and used to dynamically estimate and refine z_0 during the course of data collection. Note that Eq. (6) can also be used without any modification to solve for z_0 based on a single data point. This dynamic determination of z_0 based upon the acquired tomographic images is the essence of this proposed data collection scheme

$$z_0 = \frac{n_0 * \cos\theta * \sum_i (1 - \cos\alpha_i) * \sin\alpha_i + \sum_i \Delta x_i * \sin\alpha_i}{\cos\theta * \sum_i \sin^2\alpha_i}. \quad (6)$$

2.5. Predict-refine procedure

As previously described, z_0 is the only parameter that needs to be estimated during the data collection. This can be done with only one data point of (α, Δx) using Eq. (6). To acquire the first data point, two tilt images need to be acquired and correlated. The estimated z_0 and pre-calibrated θ and n_0 are then inserted into Eqs. (2)–(4) to predict x, y, and z translations for the third image. Once the stage has tilted to the new tilt angle, the beam and image shift coils and the objective lens current are adjusted according to the predicted Δx, Δy, and Δz values prior to taking the third tilt image. When the third image is acquired, it is cross-correlated with the second image. This yields the second data point of (α, Δx). As the first estimate of z_0 is based upon a single point and thus may not be very accurate to describe the geometry, this newly acquired data, combined with the previous one, is then used to refine the estimate for z_0 based upon Eq. (6). The refined z_0 is then used to predict x, y, and z translation for the fourth image. Repeatedly, this predict-refine procedure continues until the end of a tomography session. Based upon our own results as well as the stage calibration curves acquired using the FEI commercial tomography software, we noticed that the stage exhibits some systematic localized behaviors as a function of tilt that do not fit the global geometric rotation model. Because z_0 undergoes continuous refinement using the most recent knowledge gained from stage tilting throughout the data collection progresses, much of this aberrant behavior is absorbed into the refinement of z_0 and thus does not significantly affect the accuracy of the predictions.

3. Experimental verification

To ensure that the angle of the tilt axis is stable from day to day before the next microscope alignment has taken place, its value was measured on our T20 microscope over the span of 5 days at the same magnification based upon a thin calibration specimen. The values at the CCD camera magnification of 62 560× were −4.84°, −5.23°, and −5.13°. Similarly, n_0 was also determined based upon repeated focus measurements over the five days. The observed values were 0.03, −0.05, and 0.02 μm. Therefore it is quite reasonable to assume the angle of the tilt axis θ and the offset of the optical axis n_0 as constants between two consecutive microscope alignments.

As mentioned earlier, it is impractical to reproducibly set the sample to precisely the correct z_0. Therefore, it is critical that this approach work not only at accurate eucentric height but also within a reasonable tolerance. To verify the robustness of this approach, measurements were repeated for the same sampling point at various stage z positions above and below the eucentric height and compared with the predicted values.

To minimize the deleterious consequences of sample non-eucentricity, the data collection is divided into two loops. In the first loop, the stage is directed to tilt in the positive direction. After the maximum angle has been reached, the stage returns to its starting position and then tilts in the negative direction in the second loop of the data collection. When the stage returns to the initial angle, the sample point may not return to the center of the viewing area due to the mechanical imperfections and sample drift, even though the state of the microscope has been restored to the original setting. In order to automatically correct the shift when the stage returns to the initial angle, an image is taken at lower magnification at the initial angle prior to tilting in the positive direction. Once the stage comes back to this initial angle, the second image is taken at the same low magnification. These two images are correlated to determine the x–y displacement, which is then compensated by appropriately shifting the beam and image. While this approach has the

disadvantage of needing two extra low magnification images, the advantages of beginning at low tilt and employing a dynamic updating of parameters leads to a dramatic enhancement in robustness. And of course, using the lower magnification reduces the extra dose.

To demonstrate that the proposed approach can indeed predict x, y, and z translations with desired accuracy, image shift, and focus changes as functions of the tilt angle were measured simultaneously using the standard FEI holder on our FEI T20 transmission electron microscope equipped with a side-entry Compustage. The measured results are compared with predicted values in Figs. 2–4. Figs. 2 and 3 show x–y translations as functions of the tilt angle at three different non-eucentricity settings, corresponding to z heights errors of 0, −1, −2 μm. The tilt images were acquired every 2° starting from 0° at a final CCD magnification of 62 560×. Since the prediction procedure needs at least one data point of (α, Δx) in order to get the first estimate of z_0, as was previously described, the second image acquired at 2° was cross-correlated with the first image taken at 0°. This generated the first data point required by the prediction procedure. Therefore, the prediction of the image translation as a result of stage tilting started at the third image taken at 4°. Because of this limitation, there was no compensation to the displacement of the second image. In practice, the sample eucentricity needs to be set with sufficient accuracy to control the displacement of the second tilt image.

As can be seen from Figs. 2A and 3A, at this high magnification the sample exhibits nearly 2000 pixel shifts (∼480 nm) in x direction even at a nominal setting of $z = 0$ μm. As was pointed out in the previous section, it is impractically difficult for even a highly experienced and exacting user to tune z_0 to zero. Even very small residual values of z_0 can result in severe image shifts even at relatively low tilts. Furthermore under cryo conditions the eucentric height must be set at a remote location, again leading to sample non-eucentricity. If data collections were to begin at −70° as is done in the full pre-calibration approaches, such errors would be disastrous. As can be seen from Figs. 2 and 3, the program precisely predicted the image shifts at three distinct z heights. At $z = -2$ μm, up to ±8000 pixel shifts have been predicted within ±60 pixels corresponding to ±14.4 nm at 62 560×. The error between the measured and predicted results within ±70° is typically less than 60 pixels and rarely exceeds that value. Furthermore, this program is also found to be very robust to various angular steps. We have been able to collect tilt series every 10° even at a CCD magnification of 36 290×. To date, this program has been routinely used to collect real data for semi-thick plastic and cryo biological samples using conventional, as well as Gatan ultra-high-tilt and cryo high-tilt holders on our T20 and the cartridge holder on our F30 Polara.

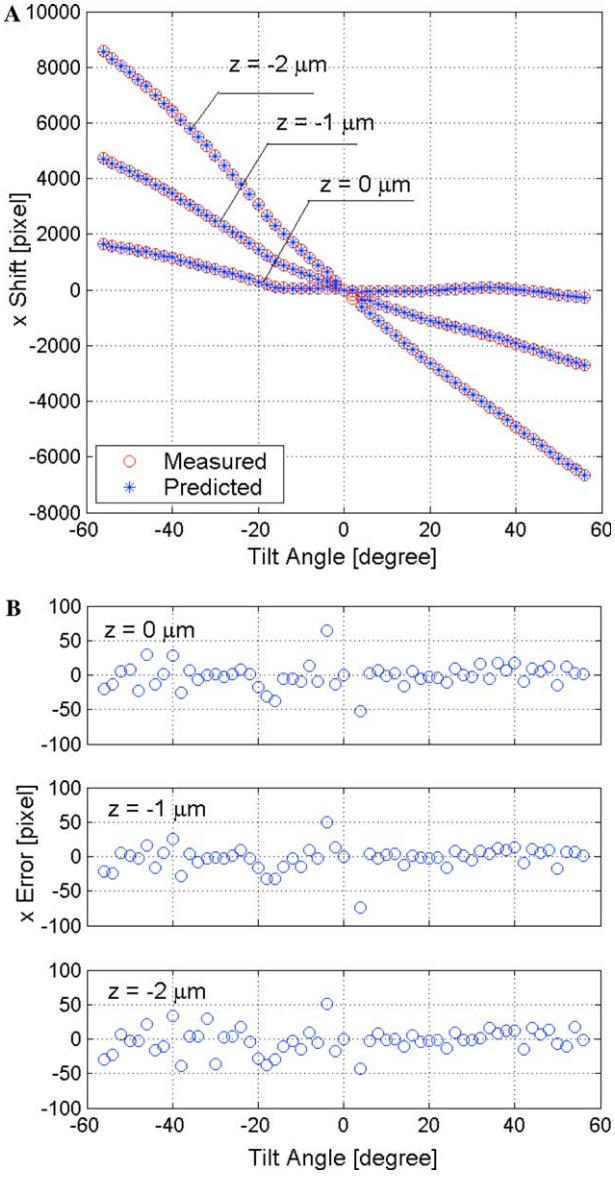

Fig. 2. (A) Measured and predicted image shift versus tilt angle in the CCD x direction at three values of mis-setting the sample eucentricity at 62 560× CCD magnification. $z = 0$ μm denotes that the sample point was manually made eucentric by an experienced microscope operator. (B) Errors between the measured and predicted values. Each pixel is 0.24 nm.

Fig. 4A shows the measured and predicted focus changes as a function of tilt angle at three z height settings. Fig. 4B presents the errors between the predicted and measured values. As in Figs. 2 and 3, $z = 0$ μm represents a manually set eucentric height. The maximum difference between the measured and predicted values is less than 0.15 μm except the left end point at −56° where a remarkable focus jump (∼0.2 μm) was measured in this particular test case. Several lines of evidence suggest that this error is actually due to an error in the measurement of the focus. First, using the same holder with other samples, such a big jump is not seen. Second, from Eq. (2) a 0.2 μm focus change due to

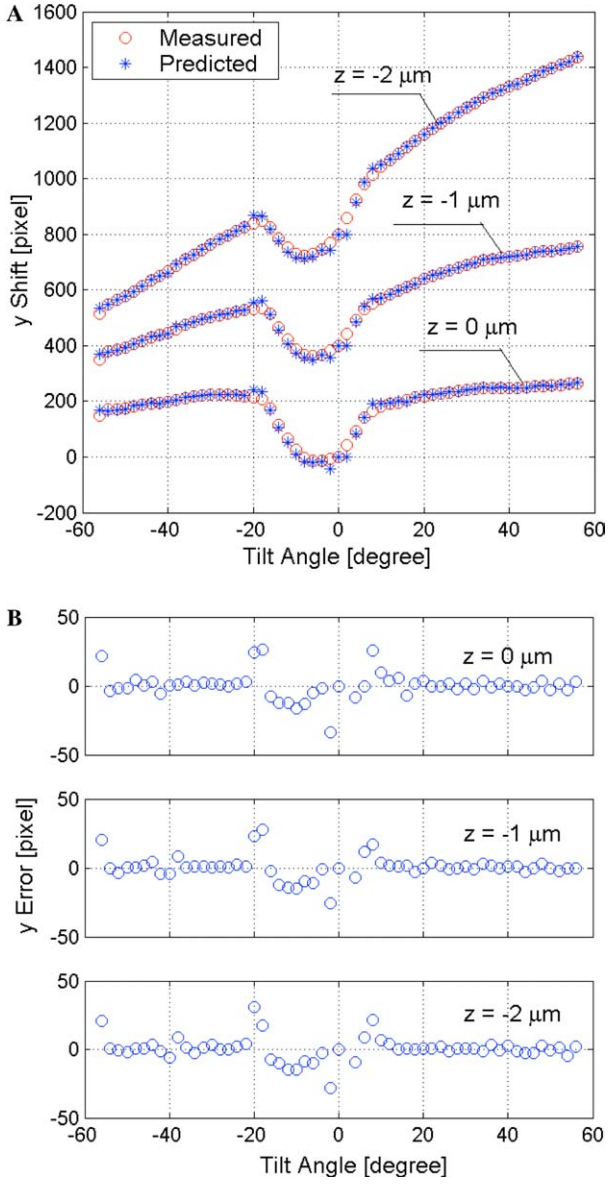

Fig. 3. (A) Measured and predicted image shift versus tilt angle in the CCD y direction at three stage z heights at 62 560× CCD magnification. Note that z is the relative stage z height or error in eucentricity. The curves are intentionally offset vertically by 400 pixels to improve clarity. (B) Errors between measured and predicted values. Each pixel is 0.24 nm.

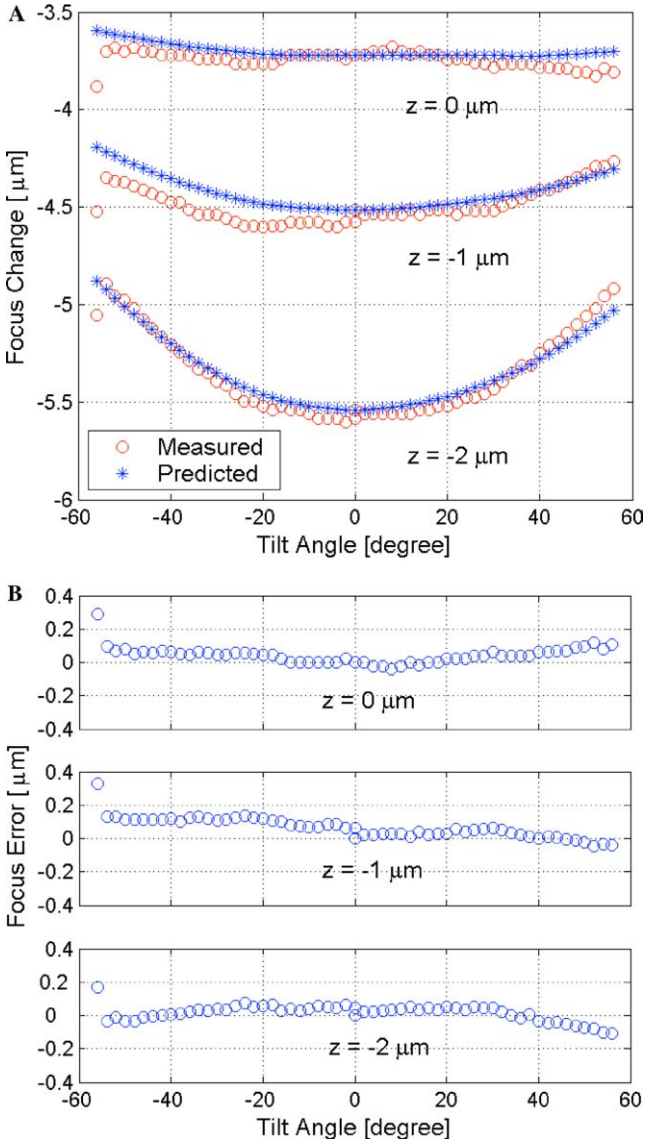

Fig. 4. (A) Measured and predicted focus change versus tilt angle at three z heights at 62 560× magnification. Note that z in the figure is the relative stage z height. (B) Errors between measured and predicted values.

a 2° change in stage tilt implies an grossly unrealistic 6 μm shift of z_0. Yet the simultaneously measured x and y shift curves show no discontinuities (Figs. 2A and 3A). Thus, we can safely exclude severe non-eucentricity and instability of the sample within the holder as causes; leading us to believe that the focus measurement at that angle may be in error. It is important to note that our approach corrects focus changes throughout data collection solely based upon predicted rather than the measured focus values. As a matter of fact, no focus measurements are performed during the entire data collection. The anomalous focus measurement is thus not a concern in the prediction.

We also noticed that Fig. 4A shows a slight discontinuity (0.001, 0.062, and 0.05 μm at $z = 0$, -1, and -2 μm, respectively) at $\alpha = 0°$. Although these discontinuities are small compared to the prediction errors, this is a consequence of dividing the data collection into two loops. When the stage returns to the starting angle from the positive end angle, mechanical imperfections make it impossible to exactly set the stage to the original x, y, and z position. As mentioned before, this is why we record images at lower magnification to allow the sample to be precisely recentered. In an effort to minimize dose we do not measure the focus when the stage returns to the initial tilt angle. As a consequence there is a slight change in z height resulting in the observed focus discontinuity.

4. System implementation

An automated data collection program has been developed based upon the aforementioned approach. A brief review regarding the system requirements as well as software architecture is presented. Since tomographic data collection critically relies on the accuracy of the CCD flat-fielding and cross-correlation calculations, it was necessary to perform these functions ourselves. The corresponding implementations are also briefly described.

The hardware portion of the entire system is composed of an FEI Tecnai computer-controlled electron microscope. In our case we use either a T20 200 kV LaB_6 instrument or a 300 kV F30 FEG with liquid He stage (Polara) and Gatan post-column energy filter. The control of the microscope is achieved via a Windows 2000 PC equipped with dual 800Mhz Pentium III processors and 1 GB memory. A four-quadrant readout bottom-mounted GATAN UltraScan CCD camera provides an imaging area of 4096×4096 pixels on the T20 and there is a Gatan 1024×1024 pixel bottom-mounted CCD camera and a 2048×2048 pixel GATAN CCD after the energy filter on the F30.

4.1. Software implementation

A scripting server provided by FEI allows for programming the stage movement and optical system in many scripting languages. Our data collection program is built on top of this server and can be roughly sketched as three functional layers. The top layer is the user interface (UI) implemented in Microsoft Visual C++. This was chosen for its rich set of tools and reusable codes for UI programming. Fig. 5 shows the data collection portion of the UI.

This portion of the UI provides for three image windows. The left one shows the image acquired at the last tilt angle, the middle for the image taken at the current tilt angle, and the third window displays the corresponding cross-correlation image. A log field continuously displays the logging information as the data collection progresses. Users can also interrupt the execution at any time if necessary.

The data collection workflow is fulfilled at the bottom layer. It is implemented in Microsoft JScript. We chose this programming language because of its simplicity in linking with the Tecnai scripting server for microscope control. Since the UI and the data collection are implemented in different programming languages, Microsoft COM technology is employed in the middle layer as a communication channel between the top and bottom layers.

4.2. Flat fielding of CCD camera

The individual responses of each pixel in the CCD array leads to fixed pattern noise in raw CCD images,

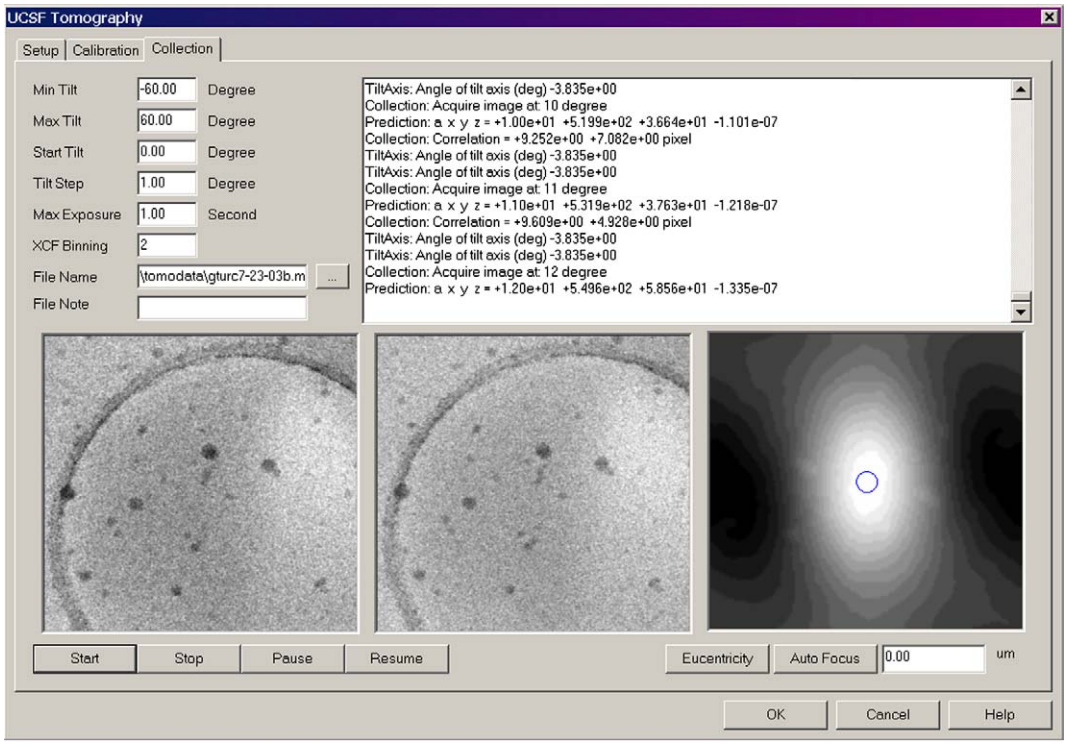

Fig. 5. User interface for the UCSF tomography data collection.

that in turn, can dominate the cross-correlation of low signal-to-noise images, especially those from cryo data collections. This problem is aggravated in four-quadrant cameras by the differing properties of the multiple readout amplifiers. It is therefore critical to flat-field the CCD array such that each pixel responds to incident electrons in an identical manner. A key concern is that the gain and offset (dark reference) for each pixel be characterized with sufficient statistical accuracy so as to not introduce additional noise sources into the image data. For this reason, a series of dark images (typically, 10 frames) are collected and averaged. The averaged dark image serves as the dark reference and is subtracted from the raw image. The gain reference is determined based upon a series of exposed images (typically, 10 frames) collected at linearly increased exposure time from which the averaged dark reference is subtracted. The gain reference for each pixel is then determined by least squares fit of the resultant intensity data. In reality, a CCD array may contain bad pixels. These may include dead pixels or pixels that do not respond linearly to incident photons or stochastic X-ray events. Those pixels are identified when the dark and gain references are built, and importantly, not included in the calculation of the reference data. When a raw image is corrected, the corresponding bad pixels are replaced with the mean intensity of neighboring pixels. Finally, for multi-quadrant cameras, it is useful to include a final correction to further minimize quadrant effects by re-scaling neighboring quadrants based on adjacent pixels across the boundary. This algorithm has been found to have excellent dynamic range. For the four-quadrant readout GATAN UltraScan CCD camera, the dark and gain references can flat-field raw images within a gray-scale range from 100 to 20 000 counts. Fig. 6 presents 4096×4096 flat fielded images of various gray-scale counts with the GATAN UltraScan CCD camera calibrated at 3000 gray-scale counts.

4.3. Cross-correlation of image displacement

For cryo low-dose data collection, the SNR of images is typically very low. The peak corresponding to the image displacement would be indistinguishable from noise peaks if the images were not filtered prior to cross-correlation. To resolve the real cross-correlation peak, a

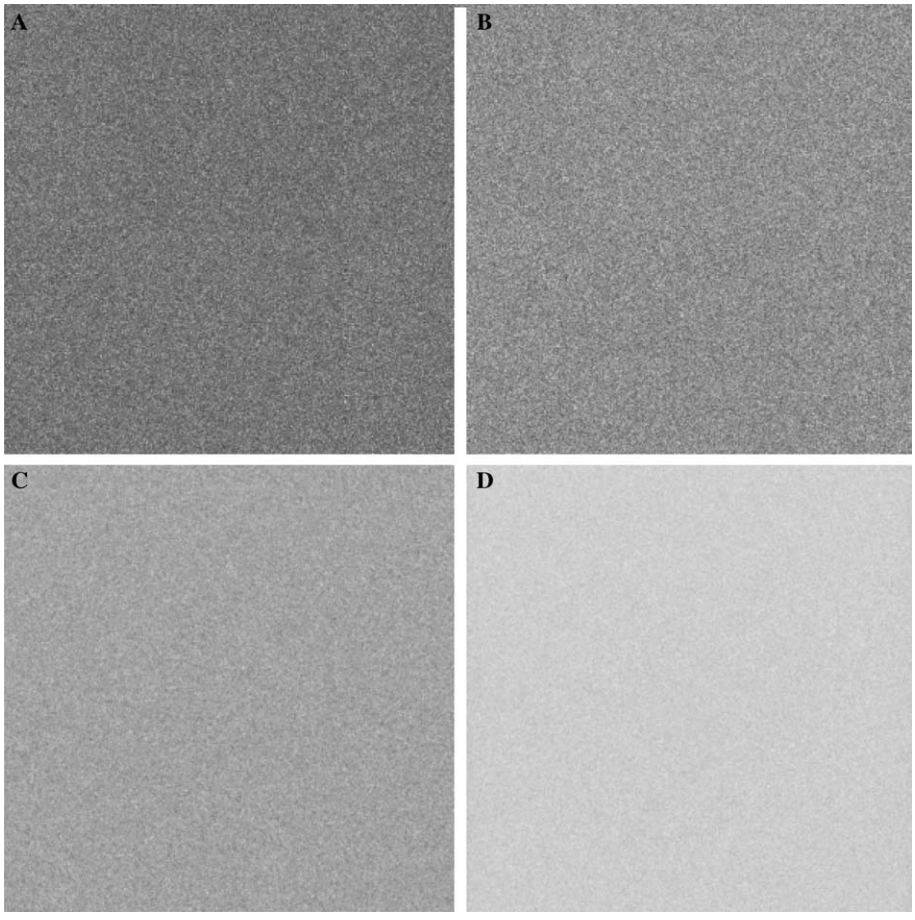

Fig. 6. Flat fielded images acquired with various doses. (A) Gray-scale count: 60, (B) gray-scale count: 120, (C) gray-scale count: 1800, and (D) gray-scale count: 18 000.

Gaussian low-pass filter in the frequency domain as given in Eq. (7) and computational image binning are employed to enhance the image SNR. Careful attention is also given to correct sample apodization. Sub-pixel accuracy is attained by interpolation. Based on our experience, the cross-correlation module is very robust and quite efficient because the cross-correlation is performed on the binned images

$$H(r) = \exp[-100 * (r/R)^2], \quad r = (x^2 + y^2)^{0.5}, \\ R = [(X/2)^2 + (Y/2)^2]^{0.5}, \tag{7}$$

where x, y represents spatial frequencies in x and y directions and X and Y are the corresponding sampling frequencies.

5. Examples of collected tomographic series

Fig. 7 presents four sections from a tilt series of gold beads deposited on holey carbon film acquired within $\pm 60°$ for every 2° at the CCD magnification of 62 560×. This experiment was performed at room temperature (21°C) using GATAN 670 high-tilt holder on our T20 microscope with a side-entry stage. It can be seen that the gold beads exhibit only a very small amount of x–y displacement among these four sections. The maximum x–y image shift of the entire data set was less than 40 pixels. The clear definition of gold beads in these four images implies that the focus was well corrected during the data collection.

Many biological samples of interest for tomography will be thicker than 0.1 μm. In reality, it is quite difficult to set an accurate eucentric height for such thick samples. As previously discussed, this predication-based approach is exceptionally tolerant of sample non-eucentricity. To verify this point, we used Epon embedded HeLa cells (for details see Belmont et al., 1987, 1989). Specimens were sectioned to a nominal thickness of 0.3 μm. Fig. 8 presents four sections extracted from the tilt series acquired at a CCD magnification of 62 560×. The maximum error in predicting x–y translation is less than 51 pixels. Again, this experiment was also performed using GATAN 670 high-tilt holder on our T20 microscope. As the embedded gold beads are well defined through the entire data set, this implies that focus change due to z movement was also well corrected.

Finally, cryo data collection was performed on poliovirus RNA-dependent RNA polymerase (Lyle et al., 2002). Samples were vitrified in liquid ethane onto Quantifoil R1.2/1.3 holey carbon films (Quantifoil, Jena, Germany). This experiment was performed on our T20 microscope using GATAN 626-DH ±70° cold stage operated at −183 °C. The liquid nitrogen was filled just below the rod in the dewar. Fig. 9 shows four sections from the data set acquired within ±60° for every 2° at CCD magnification of 36 290×. The total dose received by the sample for the entire data set was about 38 e^-/A^2. The maximum error in predicting x–y translation is less than 57 pixels. The polymerase tubes can be clearly identified on each projected image, indicating quite consistent focusing throughout the data collection.

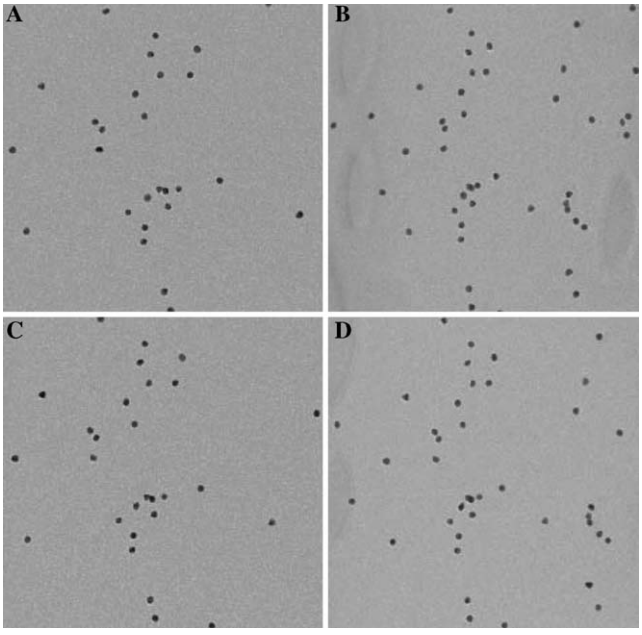

Fig. 7. Projected images acquired at magnification of 62 560× on gold beads. (A) $\alpha = 0°$, (B) $\alpha = 60°$, (C) $\alpha = -30°$, and (D) $\alpha = -60°$ The shown image area is 2048×2048 pixels.

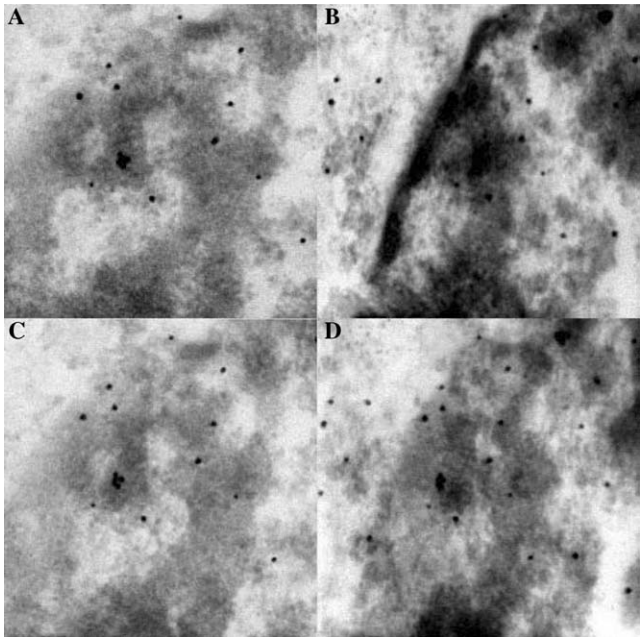

Fig. 8. Projected images acquired at magnification of 62 560× on a HeLa cell chromosome. (A) $\alpha = 0°$, (B) $\alpha = 60°$, (C) $\alpha = -30°$, and (D) $\alpha = -60°$.

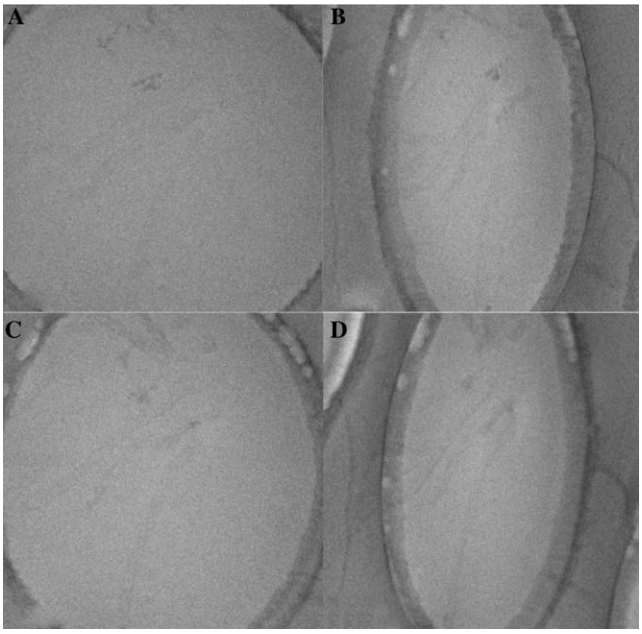

Fig. 9. Projected images acquired on cryo condition at magnification of 36 290×. (A) $\alpha = 0°$, (B) $\alpha = 60°$, (C) $\alpha = -30°$, and (D) $\alpha = -60°$ (Curtsey of Dr. John Lyle).

6. Summary and comments

As there is growing interest in electron tomography, and especially in cryo-electron tomography, this paper presents a prediction-based scheme suitable for high performance data collection. By assuming that the sample follows a simple geometric rotation as the stage tilts, we found that the image movement in the x, y, and z directions can be predicted with desired accuracy. The microscope optical system can thus be adjusted accordingly prior to taking a projected image at each tilt angle. Users are freed from a lengthy stage-calibration procedure (Ziese et al., 2002) or defining tracking and focusing areas along the tilt axis (Rath et al., 1997) prior to a data collection. Furthermore, our experiments show that this prediction-based scheme exhibits significant tolerance of sample non-eucentricity. As a result, the program is very robust, stable, and has been extensively used for both cryo and standard data collections. It should also be noted that although this software system has been extensively used to collect cryo-tomographic tilt series using a side entry GATAN 626-DH ±70° cold stage, the the stage drift has not been taken into account in the prediction of sample movement. It is undoubtedly true that stage drift can deviate the sample movement from the path defined by geometric rotation and will thus introduce error into the prediction. Owing to the constant refinement, the negative consequence of such drift is minimized. Furthermore, a preliminary test performed using the side entry GATAN 626-DH ±70° cold stage indicated that the major component of the drift is parallel to the tilt axis. Since the prediction procedure uses the sample shift normal to the tilt axis to refine the estimate of the geometric parameter, the drift should not affect significantly the precision of the prediction. We are currently investigating the ability to dynamically refine for the amount of sample drift, thereby virtually eliminating its effects on data collection at the highest resolutions.

Acknowledgments

The authors are grateful to Dr. A.J. Koster for helpful discussion and to Dr. J.M. Lyle for providing his cryo-tomographic samples and images. This work was supported by funds from the Howard Hughes Medical Institute and the W.M. Keck Advanced Microscopy Laboratory at UCSF.

References

Baumeister, W., 2002. Electron tomography: toward visualizing the molecular organization of the cytoplasm. Curr. Opin. Struct. Biol. 12, 679–684.

Belmont, S., Andrew, Braunfeld, M.B., Sedat, J.W., Agard, D.A., 1989. Large-scale chromatin structural domains within mitotic and interphase chromosomes in vivo and in vitro. Chromosoma 98, 129–143.

Belmont, S., Andrew, Sedat, J.W., Agard, D.A., 1987. A Three-dimensional approach to mitotic chromosome structure: evidence for complex hierarchial organization. J. Cell Biol. (105), 77–92.

Braunfeld, M.B., Koster, A.J., Sedat, J.W., Agard, D.A., 1994. Cryo automated electron tomography—towards high resolution reconstructions of plastic embedded structures. J. Microsc. 172 (2), 75–84.

DeRosier, D.J., Klug, A., 1968. Reconstruction of three dimensional structures from electron micrographs. Nature 217, 130–134.

Dierksen, K., Typke, D., Hegerl, R., Koster, A.J., Baumeister, W., 1992. Toward automatic electron tomography. Ultramicroscopy 40 (1), 71–87.

Dierksen, K., Typke, D., Hegerl, R., Baumeister, W., 1993. Toward automatic electron tomography II. Implementation of autofocus and low-dose procedures. Ultramicroscopy 49 (1), 109–120.

Downing, K.H., Koster, A.J., Typke, D., 1992. Overview of computer-aided electron microscopy. Ultramicroscopy 46, 189–198.

Grimm, R., Barmann, M., Hackl, W., Typke, D., Sackmann, E., Baumeister, W., 1997. Energy filtered electron tomography of ice-embedded actin and vesicles. Biophys. J. 72 (1), 482–489.

Hart, R., 1968. Electron microscopy of unstained biological material: the polytropic montage. Science 159, 1464–1467.

Koster, A.J., Chen, H., Sedat, J.W., Agard, D.A., 1992. Automated microscopy for electron tomography. Ultramicroscopy 46, 207–227.

Koster, A.J., Braunfeld, M.B., Fung, J.C., Abbery, C.K., Han, K.F., Liu, W., Chen, H., Sedat, J.W., Agard, D.A., 1993. Toward automatic three dimensional imaging of large biological structures using intermediate voltage electron microscopy. MSA Bull. 23 (2), 176–188.

Koster, A.J., Grimm, R., Typke, D., Hegerl, R., Stoschek, A., Walz, J., Baumeister, W., 1997. Perspectives of molecular and cellular electron tomography. J. Struct. Biol. 120, 276–308.

Lawrence, M.C., 1992. Least-squares method of alignment using markers. In: Frank, J. (Ed.), Electron Tomography. Plenum Press, New York, pp. 197–204.

Lyle, J.M., Bullitt, E., Bienz, K., Kirkegaard, K., 2002. Visualization and functional analysis of RNA-dependent RNA polymerase lattices. Science (296), 2218–2222.

Rath, B.K., Marko, M., Radermacher, M., Frank, J., 1997. Low-dose automated electron tomography: a recent implementation. J. Struct. Biol. 120, 210–218.

Steven, A.C., Aebi, U., 2003. The next ice age: cryo-electron tomography of intact cells. Trends Cell Biol. 13 (3), 107–110.

Ziese, U., Janssen, A.H., Murk, J.-L., Geerts, W.J.C., Van Der Krift, T., Verkleij, A.J., Koster, A.J., 2002. Automated high-throughput electron tomography by pre-calibration of image shifts. J. Microsc. 205 (2), 187–200.